PAPER

Check for updates

Remarkably stable metal–organic frameworks on an inert substrate: M-TCNQ on graphene (M = Ni, Fe, Mn)†

Zdeněk Jakub, [ID] *[a] Anna Kurowská, [ID] [a] Ondrej Herich,[a] Lenka Černá,[a]
Lukáš Kormoš,[a] Azin Shahsavar, [ID] [a] Pavel Procházka [ID] [a] and Jan Čechal [ID] [a,b]

Potential applications of 2D metal–organic frameworks (MOF) require the frameworks to be monophase and well-defined at the atomic scale, to be decoupled from the supporting substrate, and to remain stable at the application conditions. Here, we present three systems meeting this elusive set of requirements: M-TCNQ (M = Ni, Fe, Mn) on epitaxial graphene/Ir(111). We study the systems experimentally by scanning tunneling microscopy, low energy electron microscopy and X-ray photoelectron spectroscopy. When synthesized on graphene, the 2D M-TCNQ MOFs are monophase with $M_1(TCNQ)_1$ stoichiometry, no alternative structure was observed with slight variation of the preparation protocol. We further demonstrate a remarkable chemical and thermal stability of TCNQ-based 2D MOFs: all the studied systems survive exposure to ambient conditions, with Ni-TCNQ doing so without any significant changes to its atomic-scale structure or chemical state. Thermally, the most stable system is Fe-TCNQ which remains stable above 500 °C, while all the tested MOFs survive heating to 250 °C. Overall, the modular M-TCNQ/graphene system combines the atomic-scale definition required for fundamental studies with the robustness and stability needed for applications, thus we consider it an ideal model for research in single atom catalysis, spintronics or high-density storage media.

Introduction

Metal–organic frameworks (MOF) are materials consisting of metal atoms connected by organic linkers. MOFs often feature long-range ordered arrays of single metal atoms residing in an identical local environment, which makes them appealing for applications in catalysis,[1–3] spintronics, sensing[4] or quantum computing.[5,6] In principle, MOFs can be tailored for a specific function by carefully choosing a suitable metal-linker combination.

Currently, the most detailed views on the atomic-scale ordering of MOFs can be gained through on-surface synthesis and analysis of supported 2D MOFs in ultrahigh vacuum (UHV).[7] Such MOFs can feature similar structural motifs as their 3D counterparts, but their properties are generally different at the 2D level. Fundamental chemical and physical properties can be experimentally studied in staggering detail

using the on-surface approach, with recent reports providing detailed information about the nature of chemical bonds or electron correlation effects and magnetism at the atomic-scale level.[8–11] However, most of the experimental literature deals with systems supported on metal surfaces, even though it is becoming clear that to ascertain the intrinsic properties of the MOFs it is necessary to study them on supports that minimize the substrate-MOF interaction. To date, only few such systems have been reported,[12–17] the majority of which share common hurdles preventing their studies using multi-technique approaches: their structure and stoichiometry are sensitive to small variations in preparation protocols and their stability is limited to ultrahigh vacuum and temperatures of maximum few tens of °C. A simple, stable, monophase model system for multi-technique studies of intrinsic 2D MOF properties is currently missing.

Here, we present three well-defined and remarkably stable 2D MOFs supported on an inert graphene/Ir(111) substrate. As the organic linker we utilize a TCNQ molecule (7,7,8,8-tetra-cyanoquinodimethane), which is a strong electron acceptor and a popular choice for MOF synthesis both on-surface[7,9,18–22] and in solution.[23,24] TCNQ-based 2D MOFs are also intensively studied computationally,[25–31] but the simulated free-standing systems are not directly comparable to metal-supported nor

[a]CEITEC – Central European Institute of Technology, Brno University of Technology, Purkyňova 123, 61200 Brno, Czech Republic. E-mail: zdenek.jakub@ceitec.vutbr.cz
[b]Institute of Physical Engineering, Faculty of Mechanical Engineering, Brno University of Technology, Technická 2896/2, 616 69 Brno, Czech Republic
†Electronic supplementary information (ESI) available. See DOI: https://doi.org/10.1039/d2nr02017c

solution-based MOFs. To provide a more relevant model system, we chose epitaxial graphene/Ir(111) as the supporting substrate, which is chemically inert and which only shows minimal geometric and work function corrugation across the moiré unit cell.[32–34] We synthesized three different M-TCNQ 2D MOFs (M = Ni, Fe, Mn) and studied them at both atomic and mesoscopic scale using scanning tunneling microscope (STM) and low energy electron microscope (LEEM) combined with X-ray photoelectron spectroscopy (XPS). The M-TCNQ preparation protocol is very robust, and we observe only a single structure with an $M_1(TCNQ)_1$ stoichiometry for all the studied MOFs. This structure is present in 15 rotational domains on the graphene substrate, which can be described by three non-equivalent MOF/graphene rotations and mirrors. The M-TCNQ networks are remarkably chemically stable as all the tested systems survive exposures to ambient conditions, with Ni-TCNQ doing so without any significant changes to its atomic-scale structure or chemical state. The M-TCNQ MOFs were also found to be very stable thermally, but large differences were observed between the three systems: Ni-TCNQ decomposes already at 330 °C, while Fe-TCNQ remains stable even above 500 °C. Overall, we propose the graphene-supported M-TCNQ systems to be ideal models for TCNQ-based MOFs, which can provide high quality experimental benchmarks for computational studies that are typically focused on free-standing systems. With a view towards applications, highly stable monophase 2D MOFs are ideal models for research of single atom catalysis or high-density storage media.

Results and discussion

Fig. 1 shows room temperature STM images acquired on graphene/Ir(111) following M-TCNQ MOF preparation (M = Mn, Fe, Ni). In STM images shown in Fig. 1A–E, the dark areas correspond to clean Gr/Ir(111) surface, while the M-TCNQ networks are observed as the brighter areas with clearly resolved internal structure. The MOF synthesis protocol was optimized to get high monolayer coverages of the 2D MOF, and out of the tested systems the highest coverages were achieved for Ni-TCNQ. In Fig. 1A and D, the Ni-TCNQ network covers ≈75% of the surface, while monolayer coverages of up to ≈85% were achieved (shown and described further in the text). For Fe- and Mn-TCNQ systems the achievable coverages were around 60%, above which an increased number of clusters and multilayer structures were observed. The MOF structure is similar in all the tested M-TCNQ systems, a detailed STM image with an overlaid model is shown in Fig. 1F. This model is fully consistent with structures considered for free-standing M-TCNQ 2D MOFs,[29–31] as it features the same structural motifs and unit cell parameters (see further text and Table ST1 in the ESI†).
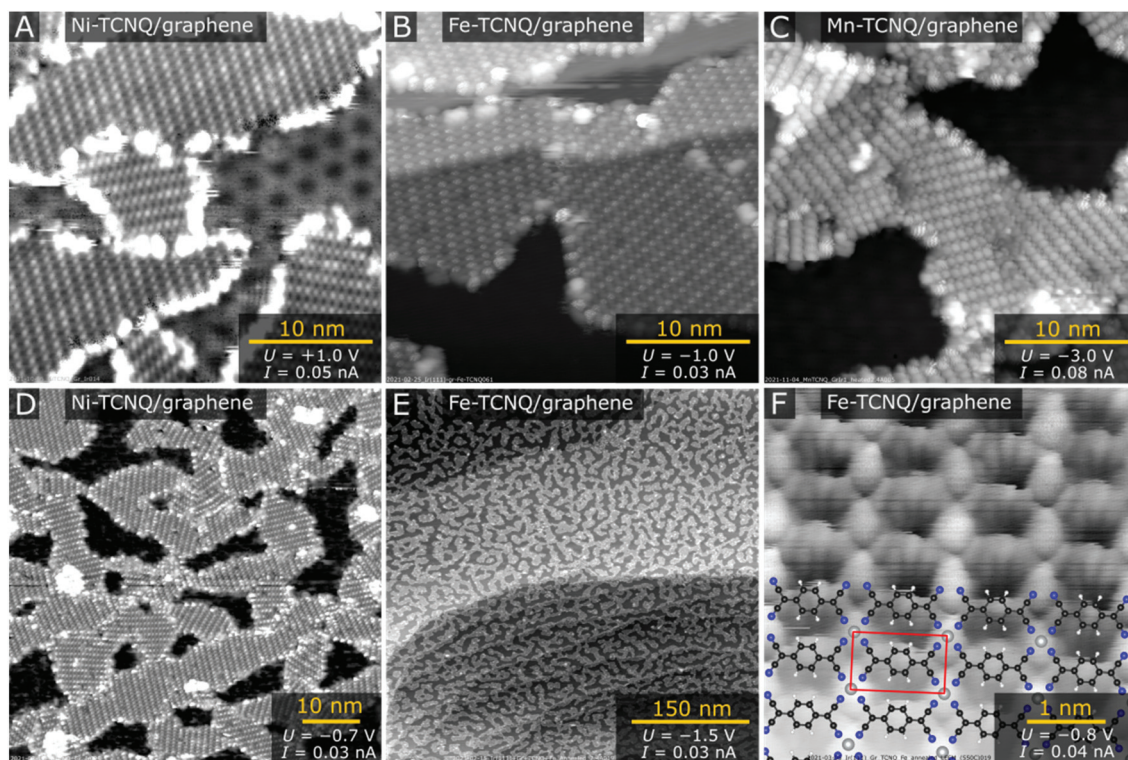

Fig. 1 STM characterization of M-TCNQ 2D MOFs supported on epitaxial graphene (M = Ni, Fe, Mn). (A–C) Detailed STM images of Ni-TCNQ (A), Fe-TCNQ (B) and Mn-TCNQ (C). (D and E) Large scale STM images of Ni-TCNQ (D) and Fe-TCNQ (E). (F) A detailed STM image showing the internal structure of Fe-TCNQ overlaid with the proposed model. All the M-TCNQ systems show similar structures. In panel (A) the graphene/Ir(111) moiré periodicity is well resolved. All the STM data were taken at room temperature.

The M-TCNQ preparation protocol on Gr/Ir(111) includes saturation of the surface kept at ≈75 °C with TCNQ, followed by co-deposition of TCNQ with transition metals at the same temperature, and subsequent post-annealing in UHV. The co-deposition temperature of ≈75 °C was chosen to increase the mobility of TCNQ molecules on the surface and to limit its residence time; XPS results show that at ≈75 °C the TCNQ slowly desorbs from Gr/Ir(111) (see Fig. S1†). The optimal post-annealing temperature varies depending on the metal; the best results were generally obtained after annealing to temperatures just below M-TCNQ decomposition. The images shown in Fig. 1A–E were measured after post-annealing temperatures of 250 °C (panels A and D), 330 °C (panels B, C and E) and 550 °C (panel F). A detailed view on the M-TCNQ thermal stability is provided further in this manuscript.

In all acquired STM images, a common metal-TCNQ structure with $M_1(TCNQ)_1$ stoichiometry is observed (proposed model shown in Fig. 1F), and for all the tested metals the structure was observed in multiple rotational domains. An analysis of large-scale STM images of Fe-TCNQ suggests the existence of 15 such rotations (Fig. S2†), and the same conclusion was drawn from LEED analysis (discussed further in the text, Fig. 2). The maximum dimensions of the individual domains range up to 60 nm (for Ni-TCNQ), while the typical size is between 10–30 nm. All the studied metal-TCNQ networks grow seamlessly over the Gr/Ir(111) step edges (Fig. 1B and Fig. S3†) and are often observed to be aligned with the longer axis of the unit cell (a_2) parallel to the Gr/Ir(111) step edge direction. This STM observation is also supported by large-scale LEEM images (Fig. S4†). From STM images calibrated to the moiré structure of the Gr/Ir(111) substrate (lattice parameter 25.2 Å (ref. 35)), the dimensions of the metal-TCNQ unit cell can be extracted, as summarized in Table ST1 in the ESI.† Within uncertainty, the dimensions are consistent with the computational predictions of free-standing M-TCNQ 2D MOFs.[30,31] Importantly, in contrast to M-TCNQ networks synthesized on metal substrates,[9,18,19,36] no alternative lateral arrangement has been observed for any of the studied M-TCNQ systems, which hints that the effect of MOF-surface interaction is indeed minimized on a graphene substrate.

In all the studied systems, a small number of apparent second layer M-TCNQ islands was observed on top of the M-TCNQ networks (Fig. S3†). These islands showed qualitatively the same structure and at the coverages shown never amounted for more than ≈7% of the 2D MOF area. In the case of Fe- and Mn-TCNQ, we occasionally observed very small areas near domain boundaries or defects in the MOF structure, which featured distinctive zig-zag appearance leading to a (2 × 1) symmetry with respect to the majority M-TCNQ structure (Fig. S3†). The origin of this appearance is currently unclear. In any case, this structure was clearly a small minority in STM datasets, and the (2 × 1) periodicity was not observed in electron diffraction patterns of any of the tested systems (Fig. 2).

Fig. 2A shows a microdiffraction pattern of Fe-TCNQ/Gr/Ir(111) measured at a primary electron energy of 16 eV. The pattern features spots originating from the Gr/Ir(111) moiré as
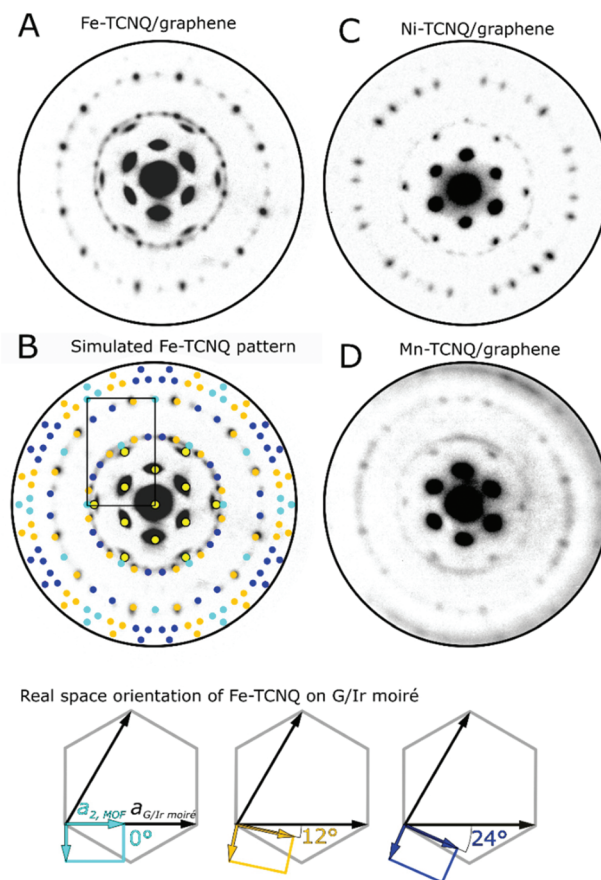

Fig. 2 Microdiffraction patterns of M-TCNQ 2D MOFs measured in a low energy electron microscope. (A and B) Fe-TCNQ pattern acquired at a primary electron energy 16 eV, the pattern originates from a circular area with a diameter of 3.7 μm. (B) Pattern simulated using parameters extracted from STM. The spots corresponding to equivalent MOF/graphene orientations are marked by the same colors. An Fe-TCNQ unit cell corresponding to 0° rotation is shown as a black rectangle. The real space orientations of the Fe-TCNQ unit cells are shown in the bottom panel. (C) Ni-TCNQ pattern (15 eV, area diameter 740 nm), (D) Mn-TCNQ pattern (8 eV, area diameter 3.7 μm). The LEED patterns were cut to show the same area in the reciprocal space.

well as the spots corresponding to the Fe-TCNQ network. Using the Fe-TCNQ dimensions extracted from STM images, the positions of the diffraction spots can be well reproduced with the Fe-TCNQ network being present in 15 rotational domains on the Gr/Ir(111) substrate (Fig. 2B). Considering the symmetries of the graphene substrate (p6mm symmetry group) and the Fe-TCNQ network (p2mm symmetry group), we identify three unique MOF/graphene orientations; these are defined by the angle between the long axis (a_2) of the MOF unit cell and the axis of the graphene unit cell (which is aligned with the Gr/Ir moiré). In the case of Fe-TCNQ, this angle is either 0° (cyan colored spots in Fig. 2B, three equivalent orientations), ≈12° (orange spots, six equivalent orientations) or ≈24° (dark blue spots, six equivalent orientations). In the experimentally observed Fe-TCNQ pattern, the set of spots corresponding to 12° rotation is more intense than the other Fe-TCNQ domains

at all electron energies between 4–20 eV (*I–V* data shown in Supplementary Movie S1†). Thus, it appears that this orientation is prevalent on the surface.

In a diffraction pattern acquired on a Ni-TCNQ system (Fig. 2C, primary electron energy 15 eV), the position of the diffraction spots is similar, but their relative intensity is different from Fe-TCNQ: the spots corresponding to ≈12° and ≈24° rotation are well-resolved and show comparable intensity, while the spots corresponding to 0° rotation are invisible. The Mn-TCNQ system was the most challenging to study using electron diffraction, because the MOF-related diffraction spots were much fainter compared to the other studied MOFs, and their shape was often smeared in the angular direction (Fig. 2D, primary electron energy 8 eV). Nevertheless, the LEED pattern is very similar to that of Fe-TCNQ, with the spots corresponding to ≈12° Mn-TCNQ being the most intense ones at all electron energies, while fainter spots corresponding to 0° and ≈24° rotation were present as well.

The chemical state and thermal stability of the M-TCNQ networks were studied by XPS and STM. Fig. 3A–D shows the N 1s and M 2p regions of XPS spectra acquired on M-TCNQ/Gr/Ir(111) after heating to various temperatures. Panels E–G show room temperature STM images of the networks after annealing to the limiting temperatures. Focusing on the N 1s XPS peak, we first measured a reference spectrum of a TCNQ monolayer on Gr/Ir(111). This reference spectrum can be well fitted by two pseudo-Voigt components, with the main component being located at 399.0 eV and a smaller, broader feature being

centered around 401.6 eV. This appearance is consistent with studies of thin and thick films of TCNQ on metal surfaces, and the broad feature located at 2.6 eV higher binding energy (BE) is commonly interpreted as a shake-up feature originating from the photoelectron interaction with the LUMO orbitals of the TCNQ molecules.[21,37,38] Thus, the presence of this shake-up indicates a neutral state of the TCNQ molecule and minimal charge transfer between the TCNQ and graphene substrate. In contrast, the spectra of M-TCNQ networks show the absence of this shake-up satellite, which is consistent with the TCNQ LUMO being involved in the bond formation with the metal atom.[11,39]

In the Ni-TCNQ case, the main N 1s component has the same position as in the case of bare TCNQ monolayer, while the Ni 2p region (Fig. 3B) shows a sharp Ni 2p$_{3/2}$ peak at 857.3 eV and a smaller component at 853.8 eV. The sharp 857.3 eV component can be assigned to the Ni-TCNQ network, but the origin of the smaller component is less clear. Possibly, it could be related to the small number of second layer islands observed in STM images (Fig. S3†), or to small Ni clusters. Upon heating to 330 °C, the N 1s signal disappears, and the Ni 2p$_{3/2}$ peak shifts to 852.8 eV, a position consistent with metallic Ni. An STM image of this surface confirms this view and shows big Ni clusters on mostly clean graphene surface, the remaining 2D islands are small and far apart (Fig. 3E, a full-sized image is provided in Fig. S5†).

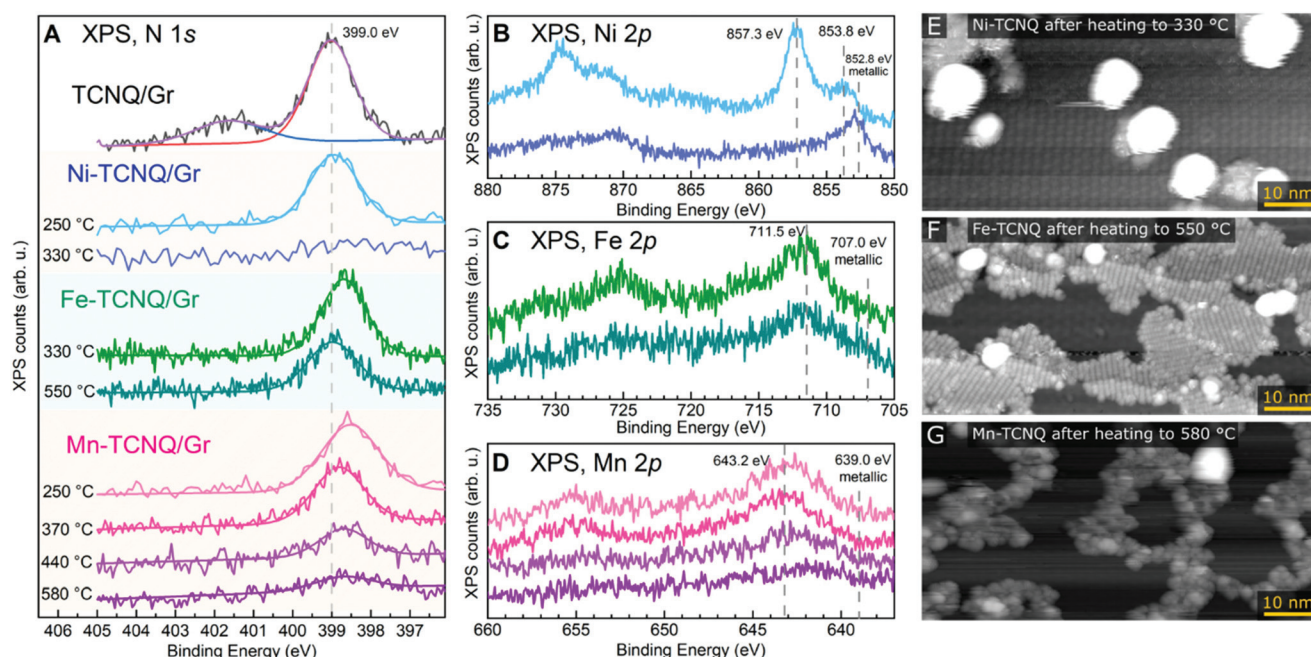The Fe-TCNQ case is curious because the spectrum taken after Fe-TCNQ preparation with post-annealing to 330 °C

Fig. 3 XPS and STM characterization of M-TCNQ 2D MOFs after annealing to various temperatures. (A) N 1s region of the XPS spectra. A monolayer of TCNQ/graphene is provided as a reference. (B) Ni 2p XPS region measured after heating of Ni-TCNQ to 250 °C and 330 °C. (C) Fe 2p XPS region measured after heating of Fe-TCNQ to 330 °C and 550 °C. (D) Mn 2p XPS region measured after heating of Mn-TCNQ between 250 °C and 580 °C. (E–G) STM images of M-TCNQ acquired after heating to the maximum temperatures shown in panel A. All the XPS data (Mg Kα) were taken in grazing emission (70° from the surface normal). All the STM data were taken at room temperature.

(a standard preparation resulting in Fe-TCNQ MOFs without any Fe clusters) shows the N 1s component significantly shifted to 398.7 eV, but upon further annealing to 550 °C this component decreases and shifts back to 399.0 eV. In the Fe 2p region, only a signal decrease is observed with no significant shift of the Fe $2p_{3/2}$ maximum (Fig. 3C). Arguably, a small peak emerges close to the metallic Fe at ≈707 eV, but the overall low signal does not allow us to claim this with certainty. An STM image acquired after the 550 °C annealing step shows islands of high-quality Fe-TCNQ network and small Fe clusters, often located at the boundaries between the Fe-TCNQ rotational domains (Fig. 3F, a full-sized image is provided in Fig. S5†).

Finally, looking at the XPS spectra of Mn-TCNQ, one can see that the N 1s component is located at 398.5 eV after annealing to 250 °C, but shifts to 398.8 eV upon heating to 370 °C (for reference, the STM image shown in Fig. 1 was taken after annealing to 330 °C). Upon further annealing up to 580 °C, the N 1s component significantly decreases and slightly shifts to 398.7 eV. Still, even after 580 °C annealing, a small N 1s signal is still detectable. In the Mn 2p region, the Mn $2p_{3/2}$ peak significantly decreases in intensity upon annealing, and after 580 °C the maximum seems to be shifted to ≈642.0 eV (Fig. 3D). An STM image taken after the 580 °C step shows a small number of clusters and rugged interconnected islands with no resolvable internal structure (Fig. 3G, a full-sized image is provided in Fig. S5†). Notably, the STM images taken at intermediate temperatures never showed images similar to Fe-TCNQ, where a coexistence of high-quality MOF with a number of small clusters is observed (Fig. 3F). Instead, the quality of the Mn-TCNQ network was gradually decreasing with increasing annealing temperature (STM images taken after annealing to intermediate temperatures are shown in Fig. S6†). Eventually, the final decomposed state is a poorly defined surface-bound network, which still contains nitrogen and non-metallic Mn.

We did not analyze the C 1s region, because the small and complex C 1s signal originating from TCNQ[37] lies very close to the much higher C 1s signal from the graphene substrate (284 eV), and the higher BE background is increased due to a dominant Ir $4d_{5/2}$ (297 eV) peak nearby (Fig. S1†).

Detailed multi-technique studies often require transfer of samples between UHV chambers with varying quality of vacuum and composition of residual gas. To test if graphene-supported M-TCNQ MOFs could survive such treatment, we tested the extreme case – exposure to air. We took the samples outside of the UHV chamber for 30 s, then put them back and annealed in UHV to remove adsorbates prior to analysis. We found that Ni-TCNQ survives air exposure without any structural, morphological, or chemical modification measurable by STM, LEEM or XPS. The large-scale STM image shown in Fig. 4A was acquired on a sample exposed to air and subsequently heated to 230 °C for 20 minutes in UHV. After this treatment the Ni-TCNQ still covers ≈85% of the graphene substrate, and the atomic-scale structure is unchanged as shown in detailed image in panel B. The LEEM diffraction pattern

(inset in Fig. 4A) shows identical spots as the pattern of a freshly prepared Ni-TCNQ, and the XPS spectrum looks very similar to the one acquired on the UHV-prepared sample (right side of Fig. 4A). STM images of Fe-TCNQ and Mn-TCNQ showed significantly decreased MOF coverage after air exposure and UHV annealing (Fig. 4C and D; the UHV annealing temperature was 330 °C in both cases), but large patches of well-ordered 2D MOFs still remained on the surface. The LEEM and XPS datasets acquired on air-exposed Fe- and Mn-TCNQ systems also look similar to the ones acquired on freshly prepared MOFs (Fig. S7†). All this indicates remarkable chemical stability of the synthesized M-TCNQ 2D MOFs.

Overall, our work shows that it is possible to synthesize high-quality monophase 2D MOFs on top of inert substrates, and with the right choice of metal and linker these MOFs can be surprisingly stable. We have found that several graphene-supported M-TCNQ MOFs share the same structure, which is present in multiple rotational domains on the graphene substrate. In 2D M-TCNQ literature, two main structural motifs are commonly reported: either the neighboring TCNQ linkers are aligned parallel to each other (as observed in this work), or alternating by 90°.[18,24,31] In some computational studies of free-standing M-TCNQ 2D MOFs, the parallel arrangement is slightly preferred,[31] but on metal-supported 2D MOFs formed by the same components the alternating structures are common.[9,11,18,19,36] One reason for this difference is the fact that TCNQ can form a strong chemical bond with the metal substrate,[22,40,41] and thus the metal substrate actively participates in the MOF formation and may significantly affect the MOF properties.[11,21] Similar effects are not expected on a graphene substrate, where strong chemical interaction with TCNQ does not take place.[42]

Even though the graphene-supported M-TCNQ 2D MOFs share the same structures, their stability and thermal decomposition mechanisms are very different. The Ni-TCNQ network decomposes readily at 330 °C, with the TCNQ most likely desorbing and the leftover Ni forming clusters on the surface. Meanwhile, the Fe-TCNQ 2D MOF is stable well above 500 °C. The decomposition mechanism of Fe-TCNQ is likely similar to that of Ni-TCNQ, with the final products being TCNQ in the gas phase and Fe clusters on the surface. The large areas of Fe-TCNQ still present at the decomposition temperature show that TCNQ remains intact within the network when the Fe-TCNQ decomposition takes place near defects or domain boundaries (Fig. 3F). Thus, for Ni- and Fe-TCNQ MOFs one can propose that the factor limiting the thermal stability is likely the CN-Metal bond. The same cannot be said for Mn-TCNQ, where both N and cationic Mn are still present after the 2D MOF decomposition, which takes place slowly from 450 °C above. One possible explanation for this is that a strong CN–Mn bond might weaken the intermolecular bonds within TCNQ. Then, the TCNQ linkers might decompose first, leaving behind Mn cyanides. Alternatively, it is possible that the Mn-TCNQ system with intact TCNQ slowly evolves into a 3D Mn-TCNQ MOF which might be thermodynamically preferred.
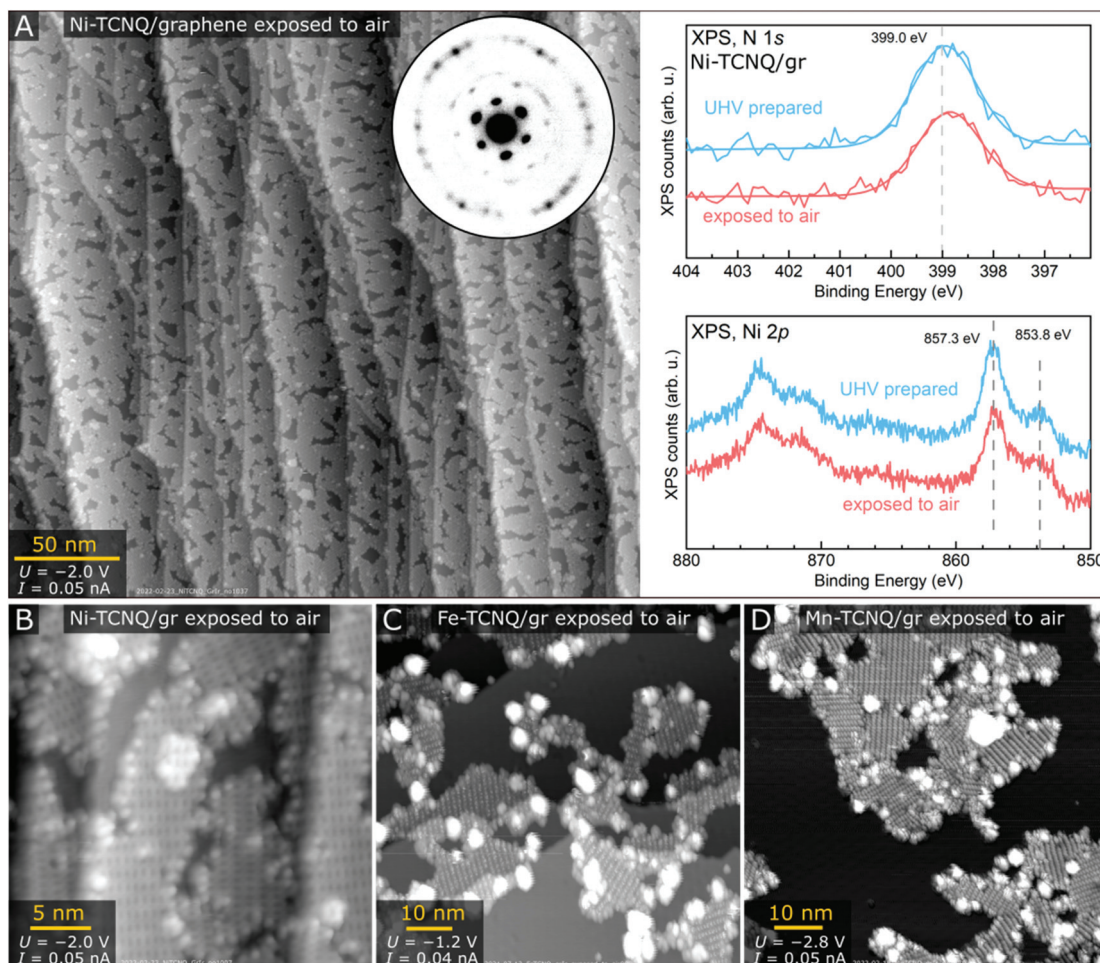
Fig. 4 Analysis of M-TCNQ/graphene systems after exposure to air. (A) STM, LEED and XPS data acquired on Ni-TCNQ/gr after exposure to air followed by 20 minutes UHV annealing to 230 °C. A large-scale STM image shows ≈85% coverage of Ni-TCNQ, while the LEED (15 eV) pattern shows the spot positions identical to freshly prepared Ni-TCNQ. Comparison of N 1s and Ni 2p XPS regions of freshly prepared and air-exposed sample reveals only ≈0.1 eV difference in the N 1s position, the Ni 2p region looks almost identical. (B) A detailed STM image shows the high structural quality of Ni-TCNQ after air exposure. (C and D) STM images of Fe-TCNQ and Mn-TCNQ after air exposure and UHV annealing to 330 °C for 20 minutes. The M-TCNQ coverage is significantly decreased in comparison to freshly prepared samples, but large patches of well-ordered MOFs remain.

Finally, we have tested the chemical stability of graphene-supported M-TCNQ 2D MOFs by exposing them to ambient conditions and re-analyzing them by surface science techniques in vacuum. The results are highly encouraging, as we found that Ni-TCNQ is a remarkably stable system, surviving air exposure without any structural, morphological, or chemical modification measurable by STM, LEED and XPS. The Fe- and Mn-TCNQ 2D MOFs were found to survive ambient exposures too, but clear evidence of partial decomposition was observed.

The modular nature of 2D MOFs implies a large degree of variability and tunability: in our study we have targeted just three transition metals, but many others are expected to form isostructural 2D MOFs with TCNQ linkers.[27,29,30] The large differences in chemical and thermal stability that we observed suggest it might be possible to synthesize atomically-defined 2D M-TCNQ MOFs which could be highly stable in a wide

range of application conditions, possibly even high pressure or liquid. In addition to metal substitution, the 2D MOF stability could be improved by modifying the linker molecule. A good starting point in this direction might be F4TCNQ (2,3,5,6-tetra-fluoro-7,7,8,8-tetracyanoquinodimethane), which was shown to form very similar MOFs as TCNQ both on-surface and in solution,[11,24] and compounds containing F4TCNQ were previously shown to be more stable in atmospheric conditions.[24]

In our view, the high quality and remarkable stability of Ni-TCNQ/graphene/Ir system already make this an ideal model for detailed multi-technique studies of single-atom reactivity or weak magnetic interactions between substrate-decoupled metal atoms. The graphene substrate plays mainly a decoupling role in our current study; however, going forward the graphene can be electrically or chemically doped, which will open yet another way to controllably tune the 2D MOF properties and tailor the material for specific functions.

Conclusions

We have prepared highly stable TCNQ-based 2D MOFs on an inert graphene substrate. The synthesized M-TCNQ networks cover a large fraction of the graphene substrate and grow seamlessly over the terrace edges. We demonstrate that three different TCNQ-based 2D MOFs share the same structure, and all the tested systems show remarkable thermal and chemical stability. These characteristics make the graphene-supported M-TCNQ 2D MOFs ideal model systems for multi-technique studies of intrinsic MOF properties, which are difficult to ascertain on metal substrates. Additionally, these M-TCNQ MOFs are ideal testbeds for computational studies of 2D MOF reactivity and can serve as experimental benchmark systems for a large body of existing computational literature. Aiming for applications, the M-TCNQ systems are optimally suited for research in single atom catalysis, high density storage media or molecular spintronics.

Methods

Experiments were carried out in an ultrahigh vacuum system comprising of multiple chambers interconnected by a central transfer line, separated by gate valves. The base pressure of all the chambers used in this study is below 5×10^{-10} mbar. The Ir (111) single crystals (supplied by MaTecK and SPL) were cleaned by cycles of Ar+ sputtering (1.8 keV, 10 min) and flashing up to 1350 °C followed by annealing to 1080 °C (10 min). When graphene was present on the sample prior to cleaning, the first annealing cycle took place in O_2 background (1160 °C, $p_{O_2} = 1 \times 10^{-6}$ mbar). The temperature was measured by a LumaSense IMPAC IGA 140 pyrometer with the emissivity set to 0.1.

Graphene was grown by adsorbing saturation coverage of ethylene at room temperature followed by prolonged annealing up to 1160 °C in ethylene background (4×10^{-8} mbar, 12 min) and subsequent flash annealing to 1350 °C in UHV. This protocol combines temperature programmed growth (TPG) with chemical vapor deposition (CVD),[35,43] and consistently leads to a full monolayer coverage of graphene/Ir(111). However, sometimes it resulted in a graphene monolayer featuring small rotational domains with small-angle orientations close to 0°, as evidenced by significant smearing of the graphene/Ir moiré spots observed in diffraction patterns.[44] An alternative CVD protocol was tested in which the sample was heated to 1250 °C in UHV, followed by 5×10^{-6} mbar ethylene exposure for 5–15 minutes at the same temperature. This protocol led to locally much sharper graphene/Ir moiré spots, but often resulted in a small number of areas of different large-angle orientations. The graphene/Ir substrate orientation did not seem to have a significant influence on the M-TCNQ self-assembly or stability, as similar M-TCNQ MOFs were prepared on all the tested samples (judging by STM data and LEED patterns).

For the M-TCNQ synthesis, TCNQ was thermally evaporated from a quartz crucible heated to 115 °C (MBE Komponenten OEZ), metals were evaporated from effusion cells (MBE Komponenten WEZ, HTEZ) or e-beam evaporators (SPECS EBE-1). The evaporation rate of metals was checked by a water-cooled quartz crystal microbalance. The temperature during M-TCNQ synthesis was calibrated by a special sample holder with a K-Type thermocouple attached close to the crystal surface.

Scanning tunneling microscopy images were recorded at room temperature in the constant current mode using a commercial system Aarhus 150 (SPECS) equipped with Kolibri Sensor using a tungsten tip. Distortion in the STM images was corrected to fit the known dimensions of graphene/Ir moiré unit cell. Where possible, non-linear image undistortion was corrected as described in ref. 45. Low Energy Electron Microscopy/Diffraction experiments were carried out in a SPECS FE-LEEM P90 instrument. The microdiffraction patterns were collected from the areas defined by a microdiffraction aperture, the aperture size is specified the figure captions. LEED patterns were simulated and plotted by LEEDpat 4.2.[46] X-ray Photoelectron Spectroscopy (XPS) analysis was performed on SPECS system equipped with Phoibos 150 spectrometer. Non-monochromatized Mg Kα radiation and grazing emission geometry (emission angle 70°) was employed for all the measurements to maximize surface sensitivity and minimize the contribution of the bulk Ir signal.

Data availability

The primary datasets generated during the current study are available in the Zenodo repository, **https://doi.org/10.5281/ zenodo.6557287**.

Conflicts of interest

There are no conflicts to declare.

Acknowledgements

References

1 D. Yang and B. C. Gates, *ACS Catal.*, 2019, **9**, 1779–1798.
2 H. Huang, K. Shen, F. Chen and Y. Li, *ACS Catal.*, 2020, **10**, 6579–6586.

3 V. Pascanu, G. González Miera, A. K. Inge and B. Martín-Matute, *J. Am. Chem. Soc.*, 2019, **141**, 7223–7234.

4 L. E. Kreno, K. Leong, O. K. Farha, M. Allendorf, R. P. Van Duyne and J. T. Hupp, *Chem. Rev.*, 2012, **112**, 1105–1125.

5 T. Yamabayashi, M. Atzori, L. Tesi, G. Cosquer, F. Santanni, M.-E. Boulon, E. Morra, S. Benci, R. Torre, M. Chiesa, L. Sorace, R. Sessoli and M. Yamashita, *J. Am. Chem. Soc.*, 2018, **140**, 12090–12101.

6 M. J. Graham, J. M. Zadrozny, M. S. Fataftah and D. E. Freedman, *Chem. Mater.*, 2017, **29**, 1885–1897.

7 L. Dong, Z. A. Gao and N. Lin, *Prog. Surf. Sci.*, 2016, **91**, 101–135.

8 F. Queck, O. Krejčí, P. Scheuerer, F. Bolland, M. Otyepka, P. Jelínek and J. Repp, *J. Am. Chem. Soc.*, 2018, **140**, 12884–12889.

9 N. Abdurakhmanova, A. Floris, T.-C. Tseng, A. Comisso, S. Stepanow, A. De Vita and K. Kern, *Nat. Commun.*, 2012, **3**, 940.

10 D. Kumar, J. Hellerstedt, B. Field, B. Lowe, Y. Yin, N. V. Medhekar and A. Schiffrin, *Adv. Funct. Mater.*, 2021, **31**, 2106474.

11 M. N. Faraggi, N. Jiang, N. Gonzalez-Lakunza, A. Langner, S. Stepanow, K. Kern and A. Arnau, *J. Phys. Chem. C*, 2012, **116**, 24558–24565.

12 A. Kumar, K. Banerjee, A. S. Foster and P. Liljeroth, *Nano Lett.*, 2018, **18**, 5596–5602.

13 J. Li, L. Solianyk, N. Schmidt, B. Baker, S. Gottardi, J. C. Moreno Lopez, M. Enache, L. Monjas, R. van der Vlag, R. W. A. Havenith, A. K. H. Hirsch and M. Stöhr, *J. Phys. Chem. C*, 2019, **123**, 12730–12735.

14 D. Moreno, B. Cirera, S. O. Parreiras, J. I. Urgel, N. Giménez-Agulló, K. Lauwaet, J. M. Gallego, J. R. Galán-Mascarós, J. I. Martínez, P. Ballester, R. Miranda and D. Écija, *Chem. Commun.*, 2021, **57**, 1380–1383.

15 L. Yan, O. J. Silveira, B. Alldritt, O. Krejčí, A. S. Foster and P. Liljeroth, *Adv. Funct. Mater.*, 2021, **31**, 2100519.

16 J. I. Urgel, M. Schwarz, M. Garnica, D. Stassen, D. Bonifazi, D. Ecija, J. V. Barth and W. Auwärter, *J. Am. Chem. Soc.*, 2015, **137**, 2420–2423.

17 L. Schüller, V. Haapasilta, S. Kuhn, H. Pinto, R. Bechstein, A. S. Foster and A. Kühnle, *J. Phys. Chem. C*, 2016, **120**, 14730–14735.

18 N. Abdurakhmanova, T. C. Tseng, A. Langner, C. S. Kley, V. Sessi, S. Stepanow and K. Kern, *Phys. Rev. Lett.*, 2013, **110**, 027202.

19 T.-C. Tseng, C. Lin, X. Shi, S. L. Tait, X. Liu, U. Starke, N. Lin, R. Zhang, C. Minot, M. A. Van Hove, J. I. Cerdá and K. Kern, *Phys. Rev. B: Condens. Matter Mater. Phys.*, 2009, **80**, 155458.

20 J. D. Fuhr, L. I. Robino, L. M. Rodríguez, A. Verdini, L. Floreano, H. Ascolani and J. E. Gayone, *J. Phys. Chem. C*, 2020, **124**, 416–424.

21 L. M. Rodríguez, J. D. Fuhr, P. Machaín, H. Ascolani, M. Lingenfelder and J. E. Gayone, *Chem. Commun.*, 2019, **55**, 345–348.

22 P. Machaín, J. D. Fuhr, S. Schneider, S. Carlotto, M. Casarin, A. Cossaro, A. Verdini, L. Floreano, M. Lingenfelder, J. E. Gayone and H. Ascolani, *J. Phys. Chem. C*, 2020, **124**, 18993–19002.

23 Y. Wei, X. Ren, H. Ma, X. Sun, Y. Zhang, X. Kuang, T. Yan, D. Wu and Q. Wei, *Chem. – Eur. J.*, 2018, **24**, 2075–2079.

24 B. F. Abrahams, R. W. Elliott, T. A. Hudson, R. Robson and A. L. Sutton, *CrystEngComm*, 2018, **20**, 3131–3152.

25 Y. Ying, K. Fan, X. Luo, J. Qiao and H. Huang, *Mater. Adv.*, 2020, **1**, 1285–1292.

26 Z. Deng, C. Ma, S. Yan, K. Dong, Q. Liu, Y. Luo, Y. Liu, J. Du, X. Sun and B. Zheng, *J. Mater. Chem. A*, 2021, **9**, 20345–20349.

27 Q. Deng, T. Wu, G. Chen, H. A. Hansen and T. Vegge, *Phys. Chem. Chem. Phys.*, 2018, **20**, 5173–5179.

28 N. Wang, L. Feng, Y. Shang, J. Zhao, Q. Cai and P. Jin, *RSC Adv.*, 2016, **6**, 72952–72958.

29 Q. Deng, J. Zhao, T. Wu, G. Chen, H. A. Hansen and T. Vegge, *J. Catal.*, 2019, **370**, 378–384.

30 J.-H. Liu, L.-M. Yang and E. Ganz, *J. Mater. Chem. A*, 2019, **7**, 3805–3814.

31 Y. Ma, Y. Dai, W. Wei, L. Yu and B. Huang, *J. Phys. Chem. A*, 2013, **117**, 5171–5177.

32 C. Busse, P. Lazić, R. Djemour, J. Coraux, T. Gerber, N. Atodiresei, V. Caciuc, R. Brako, A. T. N'Diaye, S. Blügel, J. Zegenhagen and T. Michely, *Phys. Rev. Lett.*, 2011, **107**, 036101.

33 S. K. Hämäläinen, M. P. Boneschanscher, P. H. Jacobse, I. Swart, K. Pussi, W. Moritz, J. Lahtinen, P. Liljeroth and J. Sainio, *Phys. Rev. B: Condens. Matter Mater. Phys.*, 2013, **88**, 201406.

34 S. J. Altenburg and R. Berndt, *New J. Phys.*, 2014, **16**, 053036.

35 A. T. N'Diaye, J. Coraux, T. N. Plasa, C. Busse and T. Michely, *New J. Phys.*, 2008, **10**, 043033.

36 X. Q. Shi, C. Lin, C. Minot, T.-C. Tseng, S. L. Tait, N. Lin, R. Q. Zhang, K. Kern, J. I. Cerdá and M. A. Van Hove, *J. Phys. Chem. C*, 2010, **114**, 17197–17204.

37 M. J. Capitán, J. Álvarez and C. Navio, *Phys. Chem. Chem. Phys.*, 2018, **20**, 10450–10459.

38 J. M. Lindquist and J. C. Hemminger, *J. Phys. Chem.*, 1988, **92**, 1394–1396.

39 M. J. Capitán, J. Álvarez, C. Navío and R. Miranda, *J. Phys.: Condens. Matter*, 2016, **28**, 185002.

40 T.-C. Tseng, C. Urban, Y. Wang, R. Otero, S. L. Tait, M. Alcamí, D. Écija, M. Trelka, J. M. Gallego, N. Lin, M. Konuma, U. Starke, A. Nefedov, A. Langner, C. Wöll, M. Á. Herranz, F. Martín, N. Martín, K. Kern and R. Miranda, *Nat. Chem.*, 2010, **2**, 374–379.

41 P. J. Blowey, S. Velari, L. A. Rochford, D. A. Duncan, D. A. Warr, T. L. Lee, A. De Vita, G. Costantini and D. P. Woodruff, *Nanoscale*, 2018, **10**, 14984–14992.

42 I. S. S. de Oliveira and R. H. Miwa, *J. Chem. Phys.*, 2015, **142**, 044301.

43 J. Coraux, A. T. N'Diaye, M. Engler, C. Busse, D. Wall, N. Buckanie, F.-J. Meyer zu Heringdorf, R. van Gastel, B. Poelsema and T. Michely, *New J. Phys.*, 2009, **11**, 023006.

44 K. M. Omambac, H. Hattab, C. Brand, G. Jnawali, A. T. N'Diaye, J. Coraux, R. van Gastel, B. Poelsema, T. Michely, F.-J. Meyer zu Heringdorf and M. Horn-von Hoegen, *Nano Lett.*, 2019, **19**, 4594–4600.

45 J. I. J. Choi, W. Mayr-Schmölzer, F. Mittendorfer, J. Redinger, U. Diebold and M. Schmid, *J. Phys.: Condens. Matter*, 2014, **26**, 225003.

46 K. E. Hermann and M. A. van Hove, *LEEDPat, version 2.4*, 2014.